Limnol. Oceanogr., 55(6), 2010, 2317–2330

doi:10.4319/lo.2010.55.6.2317

Variations in the optical properties of a particle suspension associated with viral infection of marine bacteria

Julia Uitz,[a,*] Dariusz Stramski,[a] Anne-Claire Baudoux,[b,1] Rick A. Reynolds,[a] Vanessa M. Wright,[a] Jean Dubranna,[a,2] and Farooq Azam[b]

[a] Scripps Institution of Oceanography, Marine Physical Laboratory, University of California–San Diego, La Jolla, California
[b] Scripps Institution of Oceanography, Marine Biology Research Division, University of California–San Diego, La Jolla, California

Abstract

A laboratory experiment was conducted to examine the temporal dynamics of the particle size distribution (PSD) and associated optical variability caused by viral infection of marine heterotrophic bacteria. The PSD covering a broad range of particle size from $\approx$ 50 nm to 200 μm was measured in parallel with the spectral particulate absorption and beam attenuation coefficients, from which the particulate scattering coefficient, $b_p(\lambda)$, was determined. Within 12 h following infection, the host bacterial population collapsed, viral abundance increased, and submicron particles were produced as bacteria were disrupted and cell debris released, resulting in a large decrease in $b_p(\lambda)$ seen as an almost complete clearing of the particle suspension. Throughout the remainder of the experiment, significant changes in the PSD occurred primarily within the size range of relatively large particles (> 4 μm), likely as a result of the aggregation of smaller-sized particles originating from the host lysis. The PSD data were used as input for Mie scattering calculations to evaluate the effects of these particle dynamics in terms of relative contributions of different particle size classes to the scattering and backscattering coefficients. This analysis showed a significant increase in the effect of particle aggregation on light scattering during the second and third days after infection. Viral lysis of bacteria and subsequent particle dynamics produce large variations in the PSD over a broad size range on timescales from hours to a few days, and such processes lead to correspondingly large changes in the suspension optical properties.

Processes involving optical–biological interactions form the basis for functioning of aquatic ecosystems. Solar radiation within the optical range of the visible electromagnetic spectrum provides energy that drives photosynthesis in phytoplankton and macroalgae, a key process supporting life. In turn, phytoplankton, other microorganisms, and nonliving biological particles suspended in water interact with light through processes of absorption and scattering, thus exerting a feedback on the propagation of light through the water column and energy availability for photosynthesis. Therefore, an understanding of how various biological particles interact with light and what their roles are in determining the inherent optical properties (IOPs) of water is of crucial interest. This understanding is also important for improving the capability to obtain information about biogeochemically important water constituents from optical measurements, including remote-sensing techniques.

Numerous studies have been devoted to the characterization of light absorption (e.g., Sathyendranath et al. 1987; Johnsen et al. 1994), scattering (e.g., Volten et al. 1998; Vaillancourt et al. 2004), and both absorption and scattering properties in parallel (e.g., Bricaud et al. 1988; Morel and Ahn 1991; Stramski et al. 2001) for a variety of phytoplankton species and some heterotrophic microorganisms. Whereas such studies provide valuable information about the interspecies and intraspecies ranges of optical properties for the specific microorganisms subject to investigation, they provide no insight into the sources of optical variability caused by dynamic interactions between many biological species of plankton populations coexisting in natural waters.

In general, the changes in IOPs of particle suspensions are driven by changes in the particle size distribution (PSD, which represents the particle concentration as a function of particle size) and particle types present within the particulate assemblages (i.e., particle properties such as shape and complex refractive index). Zooplankton grazing and lytic viral infection of bacteria and phytoplankton are prominent examples of biological interactions that result in significant transformations of particulate assemblages and their optical properties. Changes in the optical properties and size distribution of a particle suspension caused by microzooplankton grazing on cyanobacteria were demonstrated by Stramski et al. (1992). Several studies were devoted to the effects of viral-mediated mortality on the optical properties of host suspensions of marine heterotrophic bacteria (Balch et al. 2002) and cyanobacteria (Simis et al. 2005, 2007; Balch et al. 2007). Drastic reduction of particulate scattering and absorption was observed on timescales of several hours to a few days as a result of viral infection. These experiments also showed that viral infection can produce significant amounts of submicrometer particles attributable to debris of host cells. This

* Corresponding author: juitz@ucsd.edu

Present addresses:
[1] Institut Universitaire Européen de la Mer, UMR 6539, Place Nicolas Copernic, 29280 Plouzané, France
[2] Centro de Investigación Científica y de Educación Superior de Ensenada, Ensenada, Baja California, México

implies a change in the PSD, the principal determinant of IOPs. Other pathways for PSD modifications may also occur and have implications for optical properties. In particular, colloids form a dynamic pool of materials capable of major changes on short timescales, for example through particle aggregation (Chin et al. 1998; Verdugo et al. 2004). One can therefore expect that the small-sized products of viral lysis can serve as a source for the generation of larger particles.

An understanding of how biological interactions such as viral infection affect the optical properties through modifications of PSD remains limited, primarily because of the lack of measurements of PSD over a broad enough range of particle sizes that are optically significant (i.e., from the submicron size range to relatively large particle sizes on the order of 100 μm). In this study we conducted a laboratory experiment with concurrent IOP and PSD measurements to examine the question of how particle dynamics over a broad size range affects optical variability as a result of viral infection of marine heterotrophic bacteria. Over a period of 3 d we measured the beam attenuation and absorption coefficients of particle suspensions from the ultraviolet (UV) to near-infrared with high spectral resolution and the PSD from $\approx$ 50 nm to 200 μm by means of a combination of three techniques, each most suitable for a different size range but with some overlap. Using these measurements in conjunction with optical modeling, we examine how temporal changes in the PSD during our experiment affect the light-scattering budget defined by the contributions of different particle size classes to bulk scattering.

Methods

Host cells and bacteriophage—The host–virus system used in this study was the marine bacterium *Vibrio* sp. SWAT-3 (Long and Azam 2001) and the lytic Siphovirus bacteriophage strain SIO-2 isolated from seawater and characterized by A.-C. Baudoux in the Azam Laboratory. Bacteria were grown in ZoBell medium (5 g L^{-1} peptone, 1 g L^{-1} yeast extract). To avoid submicron particle contamination, the medium was prepared from a concentrated (20×) stock that was autoclaved, filtered (0.2-μm Nuclepore, Whatman), and diluted in ultrafiltered autoclaved seawater (UASW). UASW was obtained using a peristaltic pump and a VivaFlow 200 cartridge (Sartorius) equipped with a 10-kDa molecular weight cutoff polyethersulfone membrane.

Preparation of bacteriophage suspension—Culture of the bacterial host *Vibrio* sp. SWAT-3 was grown in liquid ZoBell medium overnight and infected by the bacteriophage SIO-2 by plaque assay. The virus to host ratio was adjusted to give confluent lysis on the ZoBell agar overlay plates ($\approx$ 3000 plaque-forming units [pfu] per plate). Once plaques appeared, UASW was added to the plates and viruses were eluted with rocking (60 revolutions per minute, rpm) for 1 h at room temperature. Eluates were pooled and centrifuged to remove cell debris (10,000 $\times$ *g*, 30 min, 4°C). Supernatants were further filter-sterilized using autoclaved 0.2-μm membranes (Nuclepore, Whatman) and stored at 4°C until use.

Experimental cultures—The host *Vibrio* sp. SWAT-3 was grown in 600 mL ZoBell medium for 10 h with rocking (100 rpm) at room temperature. Host cells in late exponential phase were pelleted by low-speed centrifugation (2000 $\times$ *g*, 5 min, 18°C), resuspended in 40 mL UASW, and split into two equal aliquots. One aliquot was resuspended in 200 mL of bacteriophage suspension (multiplicity of infection was $\approx$ 100 based on pfu) to prepare the infected culture. This mixture was incubated at room temperature for 15 min to let the viruses adsorb on the host membrane. The second aliquot was resuspended in 200 mL of UASW and incubated under similar conditions to prepare the control culture. After incubation, both suspensions were pelleted (2000 $\times$ *g*, 5 min, 18°C) and resuspended in 200 mL of UASW. This step was repeated twice to remove any contaminating submicron particles from both suspensions and non-adsorbed viruses from the infected suspension. Control and infected cells were finally resuspended in 580 mL of UASW.

These final infected and control cultures were incubated at room temperature under gentle agitation (60 rpm) in darkness. Samples for microscopic counts of viruses and bacteria, PSD, and optical measurements were taken every 6 h, 12 h, or 24 h during a 72-h incubation period after infection. At each sampling time, the infected culture was collected and analyzed before the control culture, which was expected to be more stable.

Virus and bacteria abundance—Viruses and bacteria were enumerated using SYBR Green I (Invitrogen) staining and epifluorescence microscopy (Noble and Fuhrman 1998). A 1-mL sample was preserved in 0.02-μm filtered formaldehyde (2% final concentration) and incubated for 15 min at 4°C. Samples were diluted to the appropriate concentration in UASW, filtered onto 0.02-μm filters (Anodisc, Whatman), rinsed with UASW, and dried on the surface of a tissue paper. Filters were then placed onto a 100-μL drop of 400-fold diluted SYBR Green I solution for 15 min in darkness before drying again on the surface of a tissue paper. Filters were mounted on slides using phosphate buffer solution : glycerol (1 : 1) and 0.01% v : v p-phenylenediamine as combined antifade and mountant. Slides were examined at 100X magnification under blue-light excitation using an Olympus epifluorescence microscope. More than 200 bacteria and viruses were typically counted in 20 fields of view.

Flow field–flow fractionation (FlFFF) coupled to multi-angle light scattering—FlFFF is a chromatographic-like technique enabling the separation of macromolecules and nanoparticles based on diffusion caused by Brownian motion, which is a particle size–related property. Details about the FlFFF technique can be found in Giddings (1993*a*). Recent studies have demonstrated the potential of FlFFF for applications to marine samples from estuaries (Wells 2004; Floge and Wells 2007), coastal waters (Vaillancourt and Balch 2000; Zanardi-Lamardo et al.

2004), and microorganism cultures (Balch et al. 2002, 2007).

In this study, we used FlFFF to fractionate the infected and control samples for the purpose of obtaining subsequent measurements of multi-angle light scattering to monitor temporal changes in the size of submicron particles. The fractionation instrument was an asymmetrical Eclipse F Separation System (Wyatt Tech.). The Eclipse consisted of a channel measuring 28.5 cm in length, 7 cm in width, and 5.5 cm in height. The channel was equipped with a 350-μm–thick spacer foil that defined the channel thickness, and a 10-kDa molecular weight cutoff regenerated cellulose membrane (Microdyn-Nadir GmbH). The flow of carrier liquid along the long axis of the channel (channel flow) and the perpendicular flow (cross flow) were both controlled by an Agilent 1100 Series isocratic pump. A Rheodyne 7225 injection valve with a 100-μL sample injection loop was used to introduce samples into the channel. The system also included an online degasser and a built-in pressure sensor.

The Eclipse system was integrated with a multi-angle light-scattering (MALS) instrument, the Dawn Enhanced Optical System (Dawn EOS, Wyatt Tech.). Our Dawn EOS is equipped with a laser operating at a wavelength of 532 nm and includes a custom built-in capability to measure scattered light with the incident laser beam polarized vertically or horizontally. With the Dawn EOS connected to the Eclipse, we measured the light scattered by fractionated samples eluting from the Eclipse within the Dawn flow cell surrounded by 18 photodetectors. This particular instrument configuration enables the simultaneous measurement of light scattering at 16 angles between 14.4° and 163.3°. Our measurements were always performed with a vertically polarized incident beam. Following the manufacturer's protocol, the 90° detector was calibrated using high-performance liquid chromatography–grade toluene (Sigma–Aldrich). The other detectors were intercalibrated (or normalized) with respect to the 90° detector by making measurements with an isotropic light scatterer, bovine serum albumin (Fisher Scientific), suspended in 10-kDa ultrafiltered seawater (USW). The calibration and normalization procedure allowed quantification of the angular pattern of light scattering by fractionated samples, which was then utilized in the estimation of particle size.

The protocol for fractionating our samples was optimized to separate particles over a relatively broad submicrometer size range ($\approx$ 50–500 nm) during a reasonably limited time period (about 1 h). A series of tests was conducted using suspensions of National Institute of Standards and Technology–traceable polystyrene latex sphere standards (Duke Scientific) ranging in size from 50 nm to 700 nm and suspensions of viruses and bacteria similar to those used in the actual experiment. The carrier solution was USW. For measurements of sphere standards, we added block copolymer surfactant Pluronic F68 (BASF; 0.1% w : v) to the carrier solution to avoid interactions between particles and the membrane in the FlFFF channel. Before use, the solution was gently filtered through a 0.2-μm polycarbonate membrane (Whatman Nuclepore). In addition, the carrier solution was always prefiltered through an in-line 0.1-μm Durapore membrane filter (Millipore) placed between the pump and the channel.

As a result of multiple test measurements, we selected the following protocol for operating the Eclipse: (1) sample injection and focusing for 3 min with injection flow of 0.2 mL min^{-1}; (2) focusing for 5 min; (3) channel flow of 1 mL min^{-1}, with gradient cross flow starting at 0.5 mL min^{-1} and decreasing linearly to 0.1 mL min^{-1} for 40 min; and (4) channel flow of 1 mL min^{-1}, with constant cross flow of 0.1 mL min^{-1} for 8 min. Elution time out of the FlFFF channel is measured from the beginning of sample injection. During the entire period (56 min) of Eclipse operation, the light-scattering measurements were made with Dawn EOS at a sampling interval of 1 s. These scattering data were collected and processed using ASTRA version 5.3.4 software (Wyatt Tech.).

Based on FlFFF principles (Giddings 1993*a*), the elution time of an eluting fraction of particles is related to the particle diffusion coefficient, which is in turn linked to the particle size. Consequently, the equivalent spherical diameter (D) of particles can be retrieved from the elution time based on a calibration curve constructed using suspensions of sphere standards of known size. This method is valid as long as elution is controlled by particle diffusion in normal-mode elution, associated primarily with Brownian motion. Nevertheless, as particle size increases, diffusion becomes weaker and eventually insignificant, so that elution can be affected by other factors, such as steric effects (Giddings 1993*b*). In such cases, larger particles may elute earlier (pre-elution) than predicted from the Brownian mode theory. Theoretically, the normal elution mode spans approximately the particle diameter range of 1 nm to 1 μm. In practice, however, the diameter at which steric elution occurs may be as low as 400–500 nm and depends on fractionation conditions (e.g., Lyven et al. 1997; von der Kammer et al. 2005).

Using the Dawn EOS as a detector connected to the fractionator enables a characterization of particle size in eluting fractions with no need for the use of particle standards. Based on light scattering theory, the particle diameter D can be retrieved for each eluting volume of sample from the angular shape of scattered light intensity (Wyatt 1998). In addition, the PSD in relative units of concentration can be determined. These determinations were made using the particle analysis module of ASTRA software with the Mie scattering model (Wyatt Tech.).

Figure 1a shows an example of an FlFFF fractogram obtained for a suspension of polystyrene latex sphere standards with a nominal D ranging from 50 to 400 nm. It is expressed as the scattering intensity at 532 nm measured at an angle of 90° with vertically polarized incident beam vs. elution time of the FlFFF channel. The first sharp peak (or void peak) is associated with the elution of particles of various sizes not being retained in the FlFFF channel and is disregarded in further analysis. The elution of particle standards results in Gaussian-type peaks that are generally well resolved from each other. A calibration curve (represented by the straight line in Fig. 1a) is obtained by linear regression between the standard nominal diameters

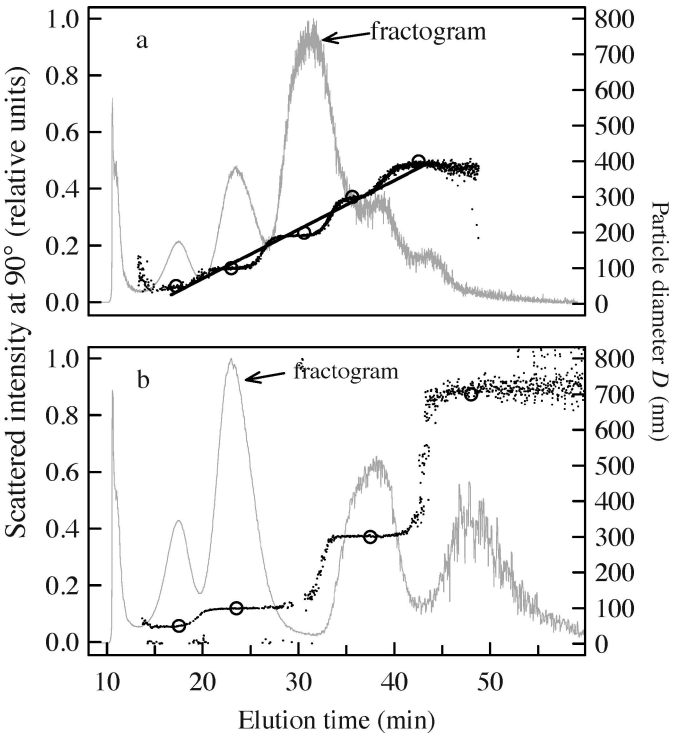

Fig. 1. Two example FlFFF fractograms (solid grey line) for different mixtures of polystyrene latex sphere standards, expressed as the scattering intensity in relative units measured at an angle of 90° with vertically polarized incident laser beam at 532 nm (the left-hand vertical axis) vs. the elution time. The open circles correspond to the nominal diameter of sphere standards (*see* the scale on the right-hand vertical axis). (a) The thick straight line represents the calibration function obtained by linear regression between the nominal diameter of standards (i.e., 50, 100, 200, 300, and 400 nm) and the elution time. The diameter of standard spheres can also be estimated from the multi-angle light scattering signal, as illustrated by a pattern of small dots connecting the open circles. (b) The example fractogram includes the data for the 700-nm diameter standards, which are inconsistent with the linear relationship between the particle diameter and elution time at smaller diameters. (a, b) The first (left-most) peak of the fractograms is disregarded in the analysis, as it corresponds to the elution of particles of various sizes that are not retained within the channel.

(i.e., 50, 100, 200, 300, and 400 nm) and the corresponding elution time. Using this calibration curve, D can be simply determined from the elution time.

When additional standards of nominal diameters in the range 500–700 nm were added to the particle suspension, steric effects were observed. In Fig. 1b, the 700-nm standard is influenced by steric effects, shows pre-elution, and thus is inconsistent with the linear calibration based on data for smaller diameters. Therefore, our FlFFF fractograms can be interpreted with confidence based on the calibration curve only for colloids smaller than $\approx$ 400–500 nm. The FlFFF data for larger colloids must be viewed with caution. We note, however, that we used another technique (Coulter counter) for sizing particles larger than 500 nm (*see* below).

As illustrated in Fig. 1, the size of the standards can also be estimated from the angular shape of MALS measurements (*see* the pattern of dots). The estimated D values are in agreement with the nominal D provided by the manufacturer for the entire size range considered (i.e., 50–700 nm). The size estimation from the MALS data becomes particularly challenging for suspensions with insufficient particle concentration. As a consequence, size retrievals from MALS in our experiment were achieved for a limited portion of the size spectrum corresponding to the peak of virus-sized particles in FlFFF fractograms ($D \approx$ 50–130 nm), in which particle concentrations and signal-to-noise ratio were sufficiently high. In addition to the main experiment we conducted several tests with suspensions of bacteria and bacterial debris produced through viral lysis, including tests with particle concentrations lower than those in the main experiment. These tests revealed that the FlFFF–MALS technique was inadequate for sizing colloids in samples when initial virus and bacterial concentrations were relatively low within a range typical of open ocean concentrations.

Coulter counter—A portion of the PSD was measured with a Beckman–Coulter Multisizer III using 20-μm and 100-μm aperture tubes. The nominal range of equivalent spherical diameter D of particles analyzed with the 20-μm aperture tube is 0.4–12 μm, but data below 0.5 μm were ignored as a result of noise effects. The size range for the 100-μm tube is 2–60 μm, which provides an overlap with the 20-μm tube. To minimize coincidence effects, particle counts were made on sufficiently dilute suspensions (i.e., diluted 4 to 200 times, depending on sampling time and aperture tube). The coincidence correction was applied when the raw PSD data were processed with the Beckman–Coulter software (Coulter AccuComp, version 3.01a). The sample volumes analyzed with the 20-μm and the 100-μm aperture tubes were 0.01 mL and 2 mL, respectively. The final PSDs were calculated by averaging three replicate measurements and subtracting an average blank measurement. The dilution factor was accounted for in the final calculations. For all measurements, USW was used as the diluent and blank.

Laser in situ scattering and transmissometry (LISST)—A LISST-100X Type-B (Sequoia Scientific) equipped with a laser operating at 532 nm was used to measure forward light scattering, which provides a means for deriving the PSD between the equivalent spherical diameters of 1 μm and 200 μm (Agrawal and Pottsmith 2000). The measurements were performed in the bench-top mode of operation. Samples were appropriately diluted to avoid multiple scattering effects (i.e., usually four times, occasionally two and eight times) and placed within a 100-mL container inserted into the optical head of the instrument. The sample chamber was covered with a dark cloth to prevent stray light effects associated with ambient illumination in the laboratory. Gentle stirring of particles was applied throughout the measurement period. The measurement of a given sample consisted of 900 repeated scans of the forward light-scattering function, collected at 1-Hz fre-

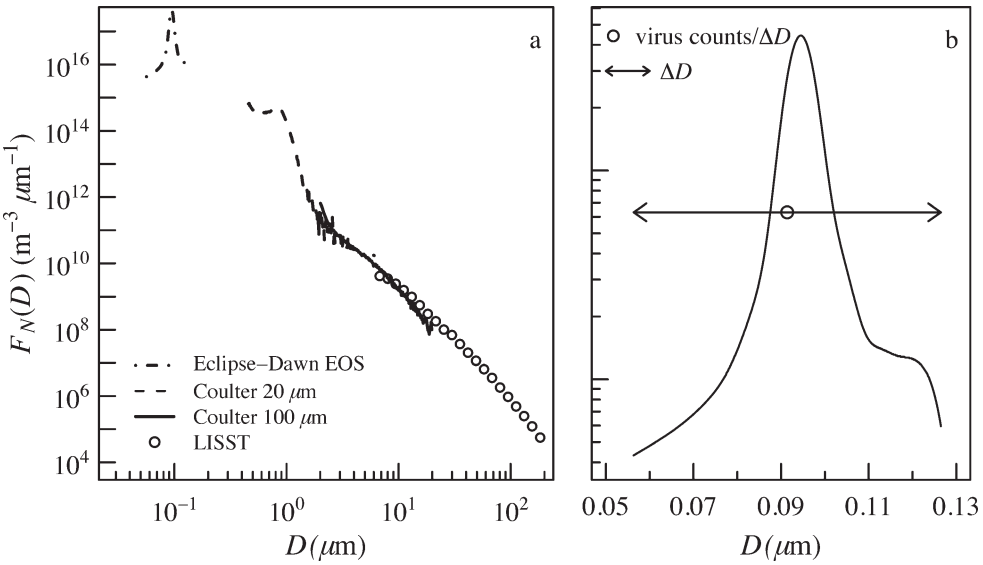

Fig. 2. (a) Example density function of particle size distribution, $F_N(D)$, obtained by combining data from the Eclipse–Dawn EOS, Coulter, and LISST measurements. The merging procedure described in the text has not been applied to these data to illustrate the overlap between the different techniques. (b) Example $F_N(D)$ function within the size range of virus population showing how the microscope counts of viruses were used to convert the relative size distribution measured with the FlFFF–MALS technique to the scaled $F_N(D)$ function over the size range ΔD (indicated by the double arrow). The open circle corresponds to the microscope determination of virus concentration divided by ΔD. The integral of the $F_N(D)$ function over the ΔD range equals the microscope-derived concentration of viruses.

quency. Blank determinations were made with USW and subtracted from sample measurements. The PSD data were subsequently averaged to produce the final PSDs. No LISST measurements were made at 6 h and 18 h after infection.

Determination of composite PSD—The PSD over the size range of equivalent spherical diameter D from 50 nm to 200 μm was determined by combining the measurements with the FlFFF–MALS, Coulter counter, and LISST instruments. An example of merging the data from these techniques is shown in Fig. 2a in terms of the density function of PSD, $F_N(D)$, expressed as the number of particles per unit volume of water and per width of the size bins. Specifically, any given value of $F_N(D)$ was calculated as $N(D)/\Delta D$, where D is the mid-point diameter of a given size bin whose width is ΔD and $N(D)$ is the number of particles per unit volume within that size bin.

The magnitude of the MALS signal was used in conjunction with D to derive the density function of PSD in relative units over the size range corresponding to the peak of virus-sized particles. This density function was then multiplied by the corresponding concentration of viruses determined from microscope counts to calculate the $F_N(D)$ in physical units of concentration per unit size interval within that portion of the size spectrum (*see* Fig. 2b).

The measurements from the Coulter counter using the 20-μm aperture tube were merged with those from the 100-μm aperture tube by averaging the data within the overlapping size region between 3 μm and 3.5 μm. Merging these two data sets provided the Coulter-based $F_N(D)$ over the 500 nm–60 μm portion of the size spectrum. To derive a portion of PSD over a range of relatively large particles (D from $\approx$ 8–15 μm to 200 μm), we assumed that the LISST data yielded the most reasonable shape of PSD within that range. The PSD magnitude in that range was obtained by scaling the LISST data to the Coulter counter data at a selected diameter. The selection of this diameter was based on a case-by-case inspection of the PSD measurements. This diameter is far from the lower and upper size limits of both instruments and falls within the range from $\approx$ 8 to 15 μm, where both data sets showed maximum consistency in PSD shape. This procedure of merging Coulter and LISST data enabled reconstructing the $F_N(D)$ over the 500 nm–200 μm size range.

We also filled the gap within the submicron range between the FlFFF–MALS data and Coulter counter data. This was done by assuming that the missing $F_N(D)$ data within the gap follow a power function model (linear regression model on log–log transformed data) between the upper limit of PSD from the FlFFF–MALS (between 110 and 130 nm, depending on the sample) and the lower limit of the Coulter-derived PSD at 500 nm. This assumption appears reasonable given the small portion of the size spectrum to which it applies and the expectation of no major features in the distribution of colloids within the considered size range (*see* Results).

The final composite $F_N(D)$ covers four orders of magnitude in particle size, which includes nearly all particles with optical significance to IOP determinations. Our $F_N(D)$ data are also characterized by high resolution with respect to particle size. The width of the size bins for

the FlFFF–MALS data is less than 0.6 nm, and for the Coulter data, the width is less than 0.15 μm. For the LISST data, the bin width varies from $\approx$ 1.6 μm within the merging size region with Coulter data to 30 μm for the last bin near 200 μm.

Spectral beam attenuation, absorption, and scattering coefficients—Optical measurements of the beam attenuation coefficient of particles, $c_p(\lambda)$, absorption coefficient of particles, $a_p(\lambda)$, and absorption coefficient of colored 'dissolved' organic matter, $a_{\mathrm{CDOM}}(\lambda)$, were made in the spectral region of 250–850 nm with a dual-beam spectrophotometer (Lambda 18, Perkin Elmer) equipped with a 15-cm Spectralon integrating sphere (RSA-PE-18, Labsphere). The symbol λ refers to light wavelength in vacuo. Below is a summary of the spectrophotometric method; a more comprehensive description can be found elsewhere (Babin and Stramski 2004; Stramski et al. 2004*b*).

For measurements of $c_p(\lambda)$, the samples were placed in a 1-cm quartz cuvette at a significant distance from the detector, and field stops were aligned within the light path to reduce the size of the beam and to limit the acceptance angle of the detector to less than 1°. The baseline spectrum representing the particle-free reference was measured on USW. Samples were appropriately diluted with USW (usually two times, although occasionally no dilution was required) to meet the criteria of single scattering regime. The values of c_p for $\lambda > 400$ nm were generally < 40 m^{-1}. These conditions ensured a sufficiently high optical signal while maintaining the effects of multiple scattering in a 1-cm cuvette at a practically undetectable level (Bricaud et al. 1988; Stramski and Piskozub 2003).

Measurements of $a_p(\lambda)$ were performed on the same samples as for $c_p(\lambda)$ but with a different measurement geometry, in which the samples in a 1-cm cuvette were placed inside the integrating sphere. For the baseline measurement, the cuvette filled with USW was used. The most significant advantage of this geometry is that the measurement of particle absorption is subject to a very small scattering error (Haardt and Maske 1987; Babin and Stramski 2002). However, minor artifacts related to scattering and reflection effects can still be observed (Babin and Stramski 2004; Stramski et al. 2004*b*). In particular, in our experiment we found a small negative offset in the measured absorbance values in the 320–400-nm spectral region. In this region the actual absorption was likely negligible, but the scattering and reflection artifacts were significant enough to produce a noticeable negative offset in the measured signal. In the far UV ($\lambda < 320$ nm), this small error was masked by the strong increase in true absorption. Nevertheless, we made a correction for the small scattering error in the UV, as follows. A negative wavelength-dependent offset was calculated by linear regression performed on data taken in the spectral range of 320–350 nm. This offset was extrapolated into the far UV and subtracted from the values of $a_p(\lambda)$ measured at $\lambda < 320$ nm. For $\lambda > 320$ nm, the measured spectrum was merely shifted upwards by a value corresponding to the negative offset, so that the resulting absorption values were set to zero. In the 400–850-nm spectral region, the measured absorption signal was practically undetectable, and, thus, in this spectral region no correction for any offset was required.

$a_{\mathrm{CDOM}}(\lambda)$ was measured on samples gently filtered through 0.2-μm polycarbonate membrane (Nuclepore, Whatman). These measurements were also made using a 1-cm cuvette placed inside the integrating sphere. Except for the far UV region, the values of $a_{\mathrm{CDOM}}(\lambda)$ were virtually zero over the entire spectral range. The USW absorbance spectra averaged from several measurements served as the baseline reference spectrum for the final calculations of $a_{\mathrm{CDOM}}(\lambda)$. As our $a_{\mathrm{CDOM}}(\lambda)$ measurement represents absorption by dissolved organic matter and particles smaller than 200 nm present in the sample, excluding molecules $<$ 10 kDa, for convenience we refer to this material as dissolved organic matter.

For each sample and each type of spectrophotometric measurement, three replicate scans of absorbance were made between 250 and 850 nm at 1-nm intervals. In each case, the result was corrected for the appropriate baseline spectrum. The individual scans were smoothed twice with a 5-nm moving average and were averaged to produce the final spectrum. The values of $c_p(\lambda)$, $a_p(\lambda)$, and $a_{\mathrm{CDOM}}(\lambda)$ were calculated by multiplying the measurements of the baseline-corrected optical density *OD* (i.e., absorbance measured in the beam attenuation or absorption setup) of the sample by ln(10) and dividing by the path length (0.01 m). The spectral scattering coefficient of particles, $b_p(\lambda)$, was calculated as the difference $c_p(\lambda) - a_p(\lambda)$.

Calculations of light-scattering budget—The temporal changes in the contribution of different particle size classes to total particulate scattering in the infected culture were examined within the framework of Mie scattering theory (Bohren and Huffman 1983). The bulk spectral scattering coefficient of a polydisperse particle suspension, $b_p(\lambda)$, can be considered as the sum of scattering by various individual particles when the suspension is sufficiently dilute. Assuming spherical homogeneous particles with a size distribution $F_N(D)$, this relationship can be written as follows (e.g., Morel and Bricaud 1986):

$$b_p(\lambda) = \int_{D_{\min}}^{D_{\max}} F_N(D)(\pi D^2/4) Q_b(\lambda, D, m) dD \qquad (1)$$

where Q_b is a dimensionless efficiency factor describing the fraction of incident light scattered by a particle with projected area $G = \pi D^2/4$ and a complex index of refraction relative to the surrounding medium, $m = n - in'$, where n and n' are the real and imaginary parts, respectively. $D_{\min}$ and $D_{\max}$ represent the minimum and maximum particle diameters, respectively.

The contributions $b_p(\lambda, D)$ of individual size classes $D \pm 0.5\Delta D$ to total $b_p(\lambda)$ were obtained as

$$b_p(\lambda, D) = F_N(D)\left(\pi D^2/4\right) Q_b(\lambda, D, m)\Delta D \qquad (2)$$

where the efficiency factors $Q_b(\lambda, D, m)$ for individual size classes were calculated using the Mie scattering code for homogeneous spheres (Bohren and Huffman 1983). The measured $F_N(D)$ of the infected culture at different

sampling times was used in these calculations. Note that

$$b_p(\lambda) = \int_{D_{\min}}^{D_{\max}} b_p(\lambda,D)\mathrm{d}D \quad (3)$$

We also calculated the corresponding cumulative distributions of $b_p(\lambda)$ according to Eq. 4:

$$C_b(\lambda,D) = \int_{D_{\min}}^{D} b_p(\lambda,D)\mathrm{d}D \left(\int_{D_{\min}}^{D_{\max}} b_p(\lambda,D)\mathrm{d}D \right)^{-1} \quad (4)$$

These scattering budget calculations were done at three wavelengths to span the entire visible range: 400, 550, and 700 nm.

Analogous relationships can be used to describe the spectral particulate backscattering coefficient, $b_{bp}(\lambda)$, in which the factor Q_b is replaced by the efficiency factor for backscattering, Q_{bb}, representing the fraction of incident light that is scattered at angles between 90° and 180°. Using these analogous relationships, we made calculations for the backscattering budget.

Prior to these scattering budget calculations, the bulk refractive index of particles was estimated, as it is required as input to the Mie code to compute $Q_b(\lambda,D,m)$ and $Q_{bb}(\lambda,D,m)$. Based upon our absorption measurements (*see* below), the particles were assumed to be non-absorbing with the imaginary part of refractive index $n'(\lambda) = 0$ for the three considered wavelengths. $b_p(\lambda)$ at each experimental sampling time was calculated iteratively from Eq. 1 using the Mie code and the measured $F_N(D)$ by systematically varying input values of the real part of the refractive index, $n(\lambda)$. From these calculations, we determined the values of $n(\lambda)$ which yielded a calculated scattering coefficient, $b_p(\lambda)$, that most closely agreed with the measured scattering coefficient.

Results

Temporal evolution of the PSD—Microscopy counts show a large increase in the abundance of viruses within 12 h after infection. The concentration of viruses started at 2.2 10^8 mL^{-1} at the beginning of the experiment ($t0$) and increased by a factor of 4 at 6 h after infection (8.8 10^8 mL^{-1} at $t6$) and by a factor of 20 at 12 h after infection (4.5 10^9 mL^{-1} at $t12$; Fig. 3). Most bacterial cells undergo lysis within 12 h, as indicated by a 230-fold reduction in their concentration, from the initial value of 8.2 10^7 mL^{-1} at $t0$ to 3.6 10^5 mL^{-1} at $t12$. After 12 h, the abundance of viruses still increases somewhat, to reach a maximum of 5.2 10^9 mL^{-1} at 24 h after infection, and then declines until the end of the experiment. After 18 h, bacterial abundance starts to increase, which is likely due to the development of virus-resistant bacteria, the growth of which may be supported by lysis products. The non-infected bacteria (control) sample did not show significant change in bacterial abundance. We note that our initial concentrations of bacteria and final concentrations of viruses are relatively high compared to typical values in open-ocean waters. For comparison purposes, the concentrations of virus-like particles in marine waters are typically within the range of 10^6–10^8 mL^{-1} (Suttle 2005). The bacterial concentrations typical of open oceans are on the order of 10^5–10^6 mL^{-1} (Cho and Azam 1990; Li 1998; Azam and Malfatti 2007), although an abundance exceeding 10^7 mL^{-1} has been reported for tropical coastal waters (Bettarel et al. 2008).

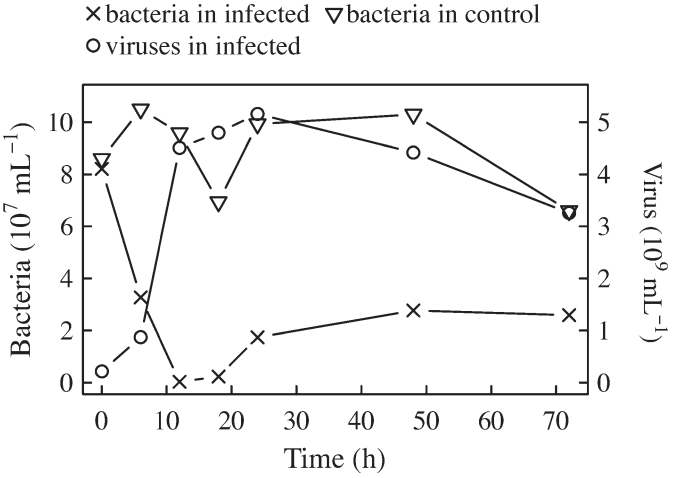

Fig. 3. Time changes in concentrations of viruses and bacteria for infected and control samples, as estimated from microscopy counts.

The FlFFF fractograms show the particle dynamics in the colloidal size range during the experiment (Fig. 4). At the beginning of the experiment ($t0$), the fractogram of the infected culture is mostly flat with low signal, especially below $D \approx 400$ nm (Fig. 4a). Then, at the sampling times $t6$, $t12$, etc., the main persistent feature is a peak centered at $D \approx 100$ nm (or 20-min elution time), which corresponds to viruses and possibly some virus-sized particles. The increase in viral abundance during the initial 6 h of the experiment is accompanied by a significant formation of colloids, larger than 100 nm. Later on, however, the abundance of colloids decreases and then remains nearly constant until the end of the experiment. This result may be related to a balance between the sources (i.e., colloid production through viral lysis) and losses of colloids (i.e., transfer to the pool of larger-sized particles through aggregation and possibly also through formation of gels, e.g., Chin et al. (1998). In contrast to the infected culture, colloids remain undetectable in the control sample throughout the experiment, as shown by the fractograms with very low flat signal (Fig. 4b).

Figure 5 illustrates the temporal changes in the density function of PSD, $F_N(D)$. No data for $t6$ and $t18$ are shown, as LISST measurements are not available for these sampling times. At the beginning of the experiment, we observe a major peak at ≈ 1 μm associated with the population of bacteria (Fig. 5a). In addition, the $F_N(D)$ shows a peak due to viruses at $D \approx 100$ nm and a steep decrease in particle concentration with D beyond the bacterial peak. The virus-related peak is shifted upwards at $t12$ compared to $t0$ and remains high throughout the rest of experiment. Within 12 h after infection, the magnitude of the bacterial peak is greatly reduced. This change is accompanied by substantial formation of relatively large

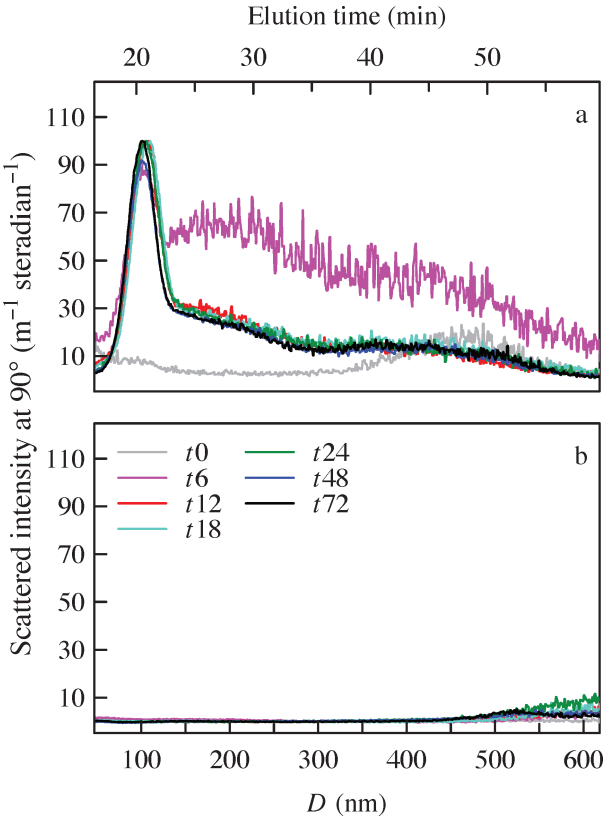

Fig. 4. FlFFF fractograms expressed as the scattering intensity measured at an angle of 90° with vertically polarized incident laser beam (532 nm) vs. particle diameter (bottom horizontal axis) or elution time (top horizontal axis) for (a) infected and (b) control samples at different sampling times, as indicated. The particle diameter D is estimated from the calibration curve using sphere standards.

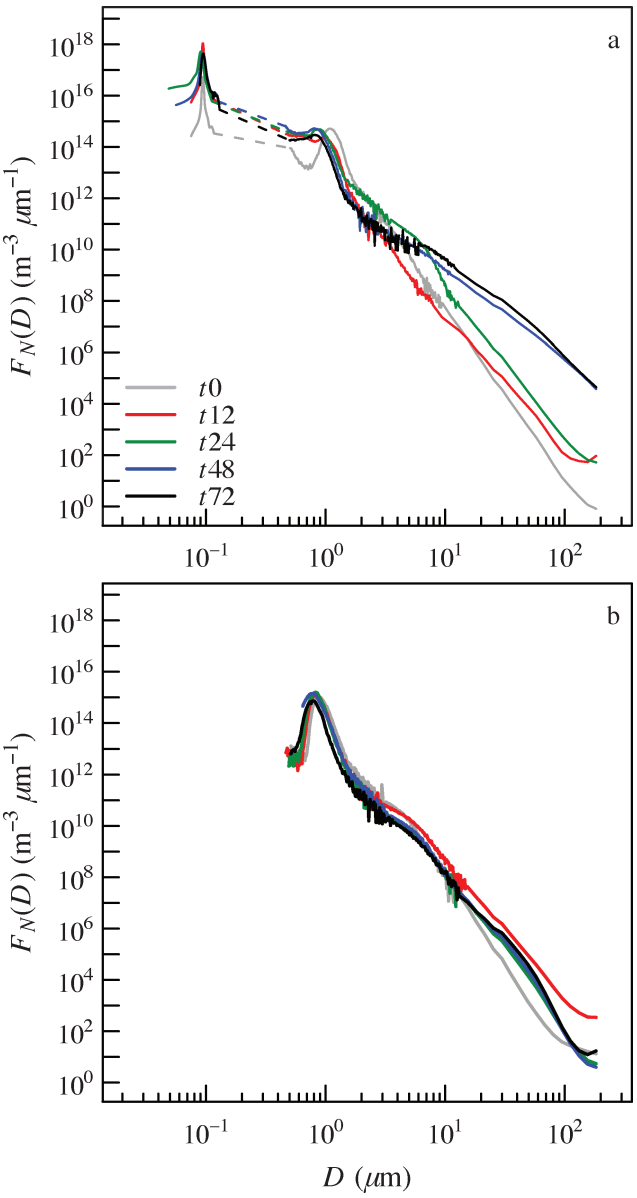

Fig. 5. Density function of particle size distribution, $F_N(D)$, for (a) infected and (b) control samples at different sampling times, as indicated.

colloidal particles within the size range of 500 nm–1 μm (i.e., the submicron portion of the size range accessible to the Coulter counter measurements). This formation likely represents the direct release of lysis products (cell debris) and the aggregation of smaller colloids that also result from lysis, as shown in the FlFFF fractograms (Fig. 4a). Although the lysis probably stops by 18–24 h after infection, the $F_N(D)$ data indicate that colloids are still present in significant numbers in the infected sample.

Important dynamics for particle sizes larger than a few micrometers throughout the experiment are also seen in Fig. 5a. There is a clear increase with time in the concentration of large-sized particles greater than ≈ 4 μm (with the exception of the first 12 h after infection). This increase is most pronounced for particles greater than 10 μm from 24 h after infection through the end of the experiment. The PSDs in the late phase of the experiment are significantly less steep compared to those in the early phase of the experiment. Our PSD data also show that the use of a simple parameterization of the broad size distribution (for example a power function with a single slope, commonly used in modeling of marine PSDs [e.g., Stramski and Kiefer 1991; Boss et al. 2001; Twardowski et al. 2001]) is not justifiable for particle suspensions undergoing viral infection of bacteria and associated particle dynamics. In addition to the features associated with viruses and bacteria themselves, our results show significant changes in the slope of the $F_N(D)$ function across the broad range of particle sizes examined.

The PSDs of control samples show much less temporal variability than those of the infected culture (Fig. 5a). Some variations in the control culture, albeit not very large and with no obvious temporal trend, are observed at particle diameters greater than 10 μm. A major peak corresponding to the population of bacteria is quite stable throughout the experiment. This peak is, however, centered at somewhat smaller diameters compared to bacteria in the infected samples (i.e., 800–900 nm, as opposed to about 1 μm). This result may be attributed to the fact that viruses

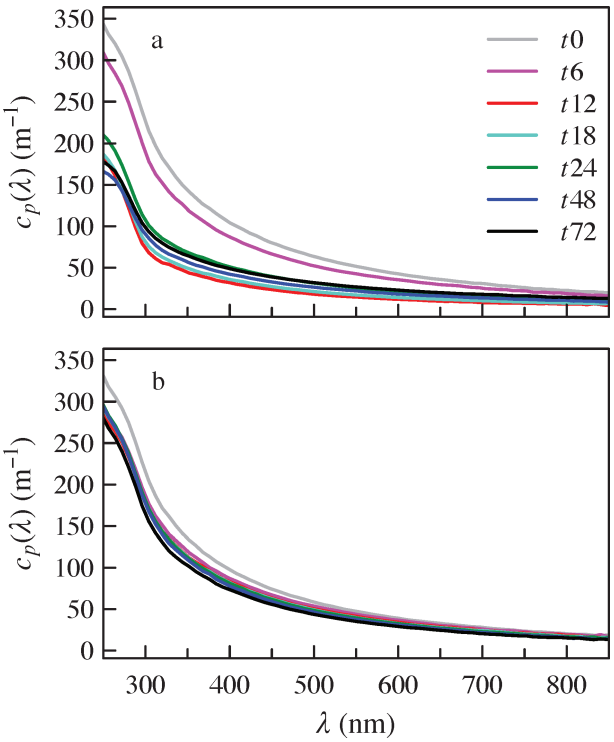

Fig. 6. Spectral particulate beam attenuation coefficient, $c_p(\lambda)$, for (a) infected and (b) control samples at different sampling times, as indicated.

rapidly adsorbed to bacterial cells in the infected culture, as well as to post-infection swelling of bacteria (Malfatti et al. 2010). Overall, the stability of the PSD for the control sample lends confidence to the interpretation of our PSD and the optical results for the infected culture that they originated primarily from the viral infection of bacteria and consequent particle dynamics.

Changes in optical properties—The observed dynamics in the PSD are accompanied by major changes in the IOPs of the infected culture, especially the particulate scattering properties. Within 12 h after infection, the spectral particulate beam attenuation coefficient, $c_p(\lambda)$, which in our experiment is virtually equivalent to the particulate scattering coefficient $b_p(\lambda)$ over most of the spectral region examined, shows a strong decrease in magnitude (Fig. 6a). For example, $c_p(440)$ and $c_p(550)$ drop by a factor of 3.4 and 3.5, respectively (Fig. 7). This indicates that the infected culture undergoes significant optical clearing as a result of the viral lysis of bacterial cells. The accompanying formation of colloidal particles does not counterbalance the loss of optical signal caused by the collapse of the bacterial population. Between 12 h and 24 h after infection, $c_p(\lambda)$ shows a moderate increase (e.g., by a factor of 1.7 and 1.8 for $c_p(440)$ and $c_p(550)$, respectively). During that period we observe some growth of (presumably resistant) bacteria (*see* Fig. 3) and an increase in the abundance of particles larger than bacteria (*see* Fig. 5a). Interestingly, further major increases in the abundance of large particles ($D > 10$ μm) observed in the late phases of the experiment

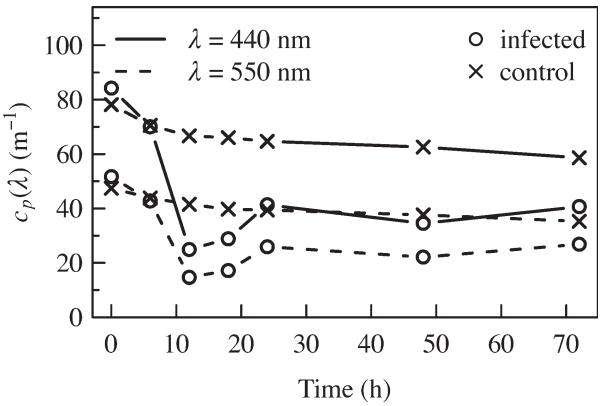

Fig. 7. Time changes in the particulate beam attenuation coefficient, $c_p(\lambda)$, at two selected wavelengths, 440 and 550 nm, for infected and control samples.

(*see* *t*48 and *t*72 in Fig. 5a) have apparently no significant effect on $c_p(\lambda)$ (Fig. 7). In contrast to the infected culture, $c_p(\lambda)$ remains fairly stable in the control sample (Figs. 6b, 7).

The spectral particulate absorption coefficient, $a_p(\lambda)$, is undetectable at wavelengths longer than $\approx$ 300 nm (Fig. 8). Thus, at these wavelengths, $c_p(\lambda) = b_p(\lambda)$, as mentioned above. At short UV wavelengths of < 300 nm, $a_p(\lambda)$ shows a strong peak (centered at $\lambda \approx 255$–260 nm), which can be attributed to absorption by proteins and nucleic acids from viruses, intact bacteria, and lysed cell debris. This UV absorption peak exhibits significant temporal changes in

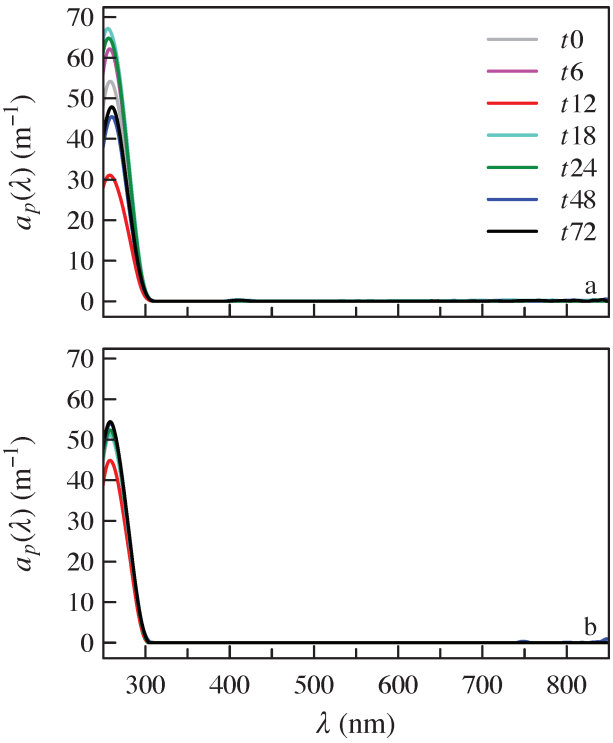

Fig. 8. Spectral particulate absorption coefficient, $a_p(\lambda)$, for (a) infected and (b) control samples at different sampling times, as indicated.

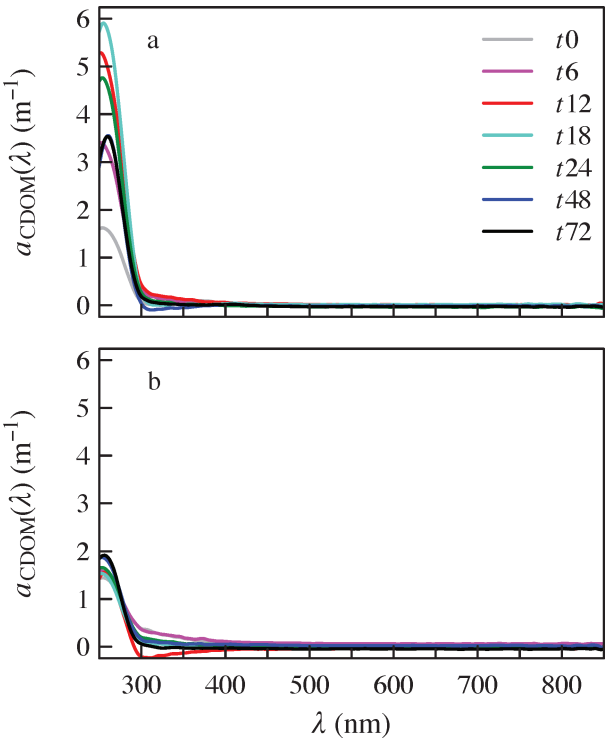

Fig. 9. Spectral absorption coefficient, $a_{CDOM}(\lambda)$, for dissolved organic matter, defined as material passing through the 200-nm filter pore size but excluding molecules < 10 kDa, for (a) infected and (b) control samples at different sampling times, as indicated.

the course of the experiment. We observe a 1.7-fold drop within 12 h after infection, which is attributed to viral lysis and decline of the bacteria population. This event is followed by a 2.2-fold increase at 18 h, likely related to the formation of large-sized particles and the growth of resistant bacteria. With the exception of some reduction of the UV peak at $t12$, the control sample shows a stable magnitude of this peak throughout the experiment (Fig. 8b).

The spectral absorption coefficient, $a_{CDOM}(\lambda)$, is also detectable only at the short UV wavelengths, but significantly lower than $a_p(\lambda)$ (Fig. 9). In that UV region, $a_{CDOM}(\lambda)$ shows a maximum centered at $\lambda \approx 252$–260 nm, which increases systematically from the beginning of the experiment until a maximum at 18 h after infection. This pattern in $a_{CDOM}(\lambda)$ is likely due to the systematic increase in the abundance of viruses over the 18-h period and the release of lysis products. As was the case with other parameters, the control sample of $a_{CDOM}(\lambda)$ shows very little variation.

Changes in the spectral slope of the particulate scattering coefficient, $b_p(\lambda)$, are generally consistent with the expectation based on the observed changes in the PSD (Fig. 10). The slope was obtained by performing a linear regression on the log–log transformed data of b_p vs. λ within the 320–820-nm spectral region. The short-wavelength UV region was excluded from the analysis to avoid the effect of absorption on the spectral shape of scattering. The steepest slope of $b_p(\lambda)$, 12 h after infection, is consistent with an

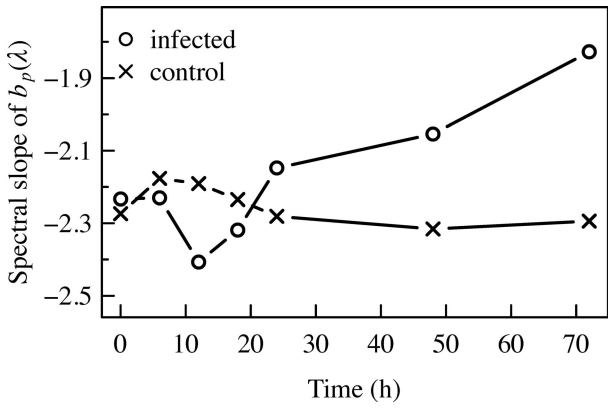

Fig. 10. Time changes in the spectral slope of the particulate scattering coefficient, $b_p(\lambda)$, for infected and control samples.

increased relative contribution of small-sized particles due to viral lysis at that sampling time. The trend by which the slope becomes gradually less steep after 12 h throughout the rest of the experiment is consistent with an increasing role of large particles.

The values of relative refractive index, n, derived from matching experimental and modeled data of b_p are within the range of values representative of biogenic particles suspended in seawater. For a light wavelength of 550 nm, a mean value of $n = 1.038$ (range, 1.034–1.043) was obtained for the five measurements comprising the sampling times $t0$, $t12$, $t24$, $t48$, and $t72$. These values agree well with previous determinations for particle suspensions of various viruses and bacteria (e.g., *see* table A.6 in Jonasz and Fournier [2007]). For the initial sampling time ($t0$), the spectral shape of $n(\lambda)$ was nearly flat, with less than an 0.3% change in value from 400 to 700 nm. The spectral slope of $n(\lambda)$ increased slightly throughout the experiment, and by 72 h the change in value between 400 and 700 nm was 2.9%. The values at 400 nm were slightly higher compared with those at 700 nm, which reasonably reflects the normal dispersion of the refractive index.

Influence of changing PSD on scattering properties—Figure 11a and b illustrate the calculated contribution to $b_p(550)$ originating from different particle sizes. For each sampling time, the results are depicted as the density function of the percent contribution with respect to particle size D (Fig. 11a). The corresponding cumulative distributions of $b_p(550)$ as a function of D are depicted in Fig. 11b. For $t0$ immediately following exposure of the bacteria to viruses, the scattering properties of the suspension were principally determined by bacterial cells (Fig. 11a). The size range 0.8–2 μm, which spans the main population of bacteria, contributed 90% of the total particle scattering and thus exhibits a very steep cumulative distribution (Fig. 11b). Particles outside this size range had only a minor contribution to scattering; particles smaller than 0.8 μm contributed only 0.6% and particles greater than 4 μm contributed 1.8% to $b_p(550)$.

These proportions changed significantly throughout the course of the experiment. The contribution by particles in the bacterial size range decreased continually over time,

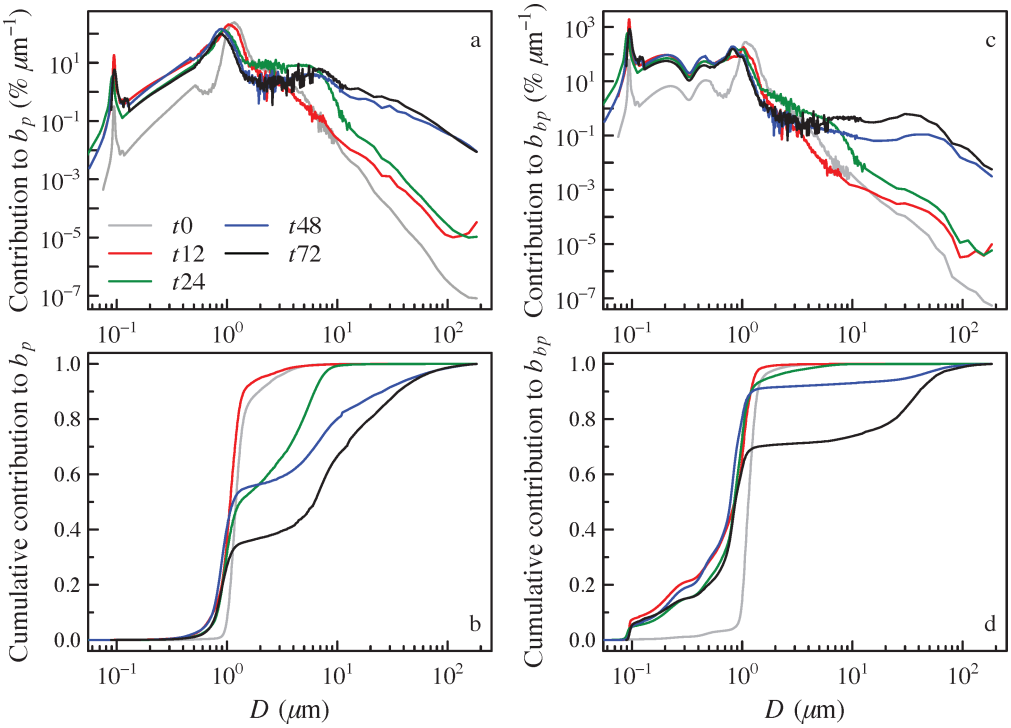

Fig. 11. (a, c) Percent contribution per micrometer bandwidth and (b, d) cumulative percent contribution as a function of particle diameter for (a, b) the particulate scattering coefficient $b_p(550)$ and (c, d) the particulate backscattering coefficient $b_{bp}(550)$ at different sampling times, as indicated.

and by 72 h after infection this size range contributed only 27% to $b_p(550)$. Increases in viral particles and small colloidal materials during the initial 12 h led to an increase in the contribution of the size range < 0.8 μm, from 0.6% to about 14%, and then this value changed little throughout the rest of the experiment. The rapid decrease in contribution of the bacterial size range following the initial 12 h was mirrored by an increase in the contribution of $>$ 4-μm particles. By the end of the experiment ($t72$), this fraction was the dominant contributor (58.6%) to $b_p(550)$.

Qualitatively similar results were observed at the other spectral bands considered in our calculations (400 and 700 nm), with differences primarily in the magnitude of contribution by the different size classes (not shown). For example, at 700 nm the contribution of the $>$ 4-μm size range increased from 2.4% to 85.4% throughout the course of the experiment. These spectral differences in magnitude arise from two causes: (1) spectral variations in the refractive index and (2) the fact that the efficiency factors are non-linear oscillatory functions of the relative size parameter D/λ over much of the size range considered in this study (e.g., Morel and Bricaud 1986).

Similar calculations were made for the particle backscattering coefficient $b_{bp}(\lambda)$, and example results for a light wavelength of 550 nm are depicted in Fig. 11c and d. Although the temporal trends observed for b_{bp} qualitatively resemble those observed for the total scattering coefficient, we note a few important differences. In general, smaller sized particles contributed an overall greater percentage to backscattering than was observed for total scattering. The contribution to $b_{bp}(550)$ of particles in the size range of $<$ 0.8 μm increased during the first 12 h, from 4% to 46%, and remained at approximately this level throughout the remainder of the experiment (Fig. 11c,d). Small particles in the size range of < 2 μm strongly dominate ($> 90\%$) the contribution to the backscattering signal throughout most of the experiment (up to $t48$). Although the contribution of larger particles > 4 μm increased over time, this fraction never became the dominant contributor to b_{bp}, reaching a maximum of $\approx 28\%$ by the end of the experiment.

We caution against an exact interpretation of these scattering budget percentages because of unavoidable uncertainties associated with the assumptions of particle sphericity and homogeneity required in the Mie theory. These assumptions can influence the prediction of scattering, especially backscattering, compared with real arbitrarily shaped, non-uniform particles (e.g., Jonasz 1987; Mishchenko et al. 2000; Clavano et al. 2007). Zaneveld and Kitchen (1995), for example, reported a more than threefold increase in backscattering for a three-layered sphere model compared with a homogeneous sphere. Despite these limitations, the combination of Mie modeling and experimental data of PSD offers a useful tool for the analysis of relative variations in the scattering budget. One may expect that the Mie assumptions do not introduce gross errors in the estimation of the relative roles of different particle sizes in the scattering budget. One reason is that the PSDs exhibit significant rapid decrease in particle concentration with increasing particle size, so the rate of this decrease, rather than variations in particle shape or heterogeneity, is likely the first-order determinant of the

scattering budget. In addition, the Mie assumptions were applied in our calculations uniformly to all particle sizes. We also note that a similar approach to estimating a scattering budget, although with more limited data of PSD, was recently used within the context of viral infection of filamentous cyanobacteria (Simis et al. 2007).

Discussion

In this study we describe changes in the optical properties of a particle suspension in response to viral infection of marine bacteria, and we interpret these optical results in terms of modifications in the PSD over a broad particle size range from about 50 nm to 200 μm. Our results show large variations in the PSD and, consequently, in the optical properties of the suspension. As is true for any laboratory experiment, the conditions of our experiment differed in some aspects from typical natural conditions, including the relatively high initial concentration of bacterial cells. Whereas no quantitative conclusions directly applicable to natural environments can be claimed based on our laboratory observations, we suggest that similar qualitative patterns in particle dynamics and associated optical variability may occur in natural waterbodies. Importantly, we emphasize that the laboratory experimental designs provide the only practical means of addressing a specific process of particle dynamics, such as viral infection of bacteria, and its influences on optics under controlled conditions with no significant interference of many other optically significant water constituents and their interactions.

Although viruses have long been recognized as a negligible direct source of light scattering in typical oceanic conditions (Stramski and Kiefer 1991; Balch et al. 2000), their potentially important optical effect has been linked to rapid infection and lysis of larger, optically significant cells (Balch et al. 2002; Simis et al. 2005). Much interest in virus-induced optical changes has been driven by the effects of the formation of submicron particles on backscattering properties (Balch et al. 2002, 2007; Simis et al. 2007). Such small-sized particles have been suggested to be an important source of backscattering in typical oceanic situations, with possible implications for optical remote sensing of the ocean (Morel and Ahn 1991; Stramski and Kiefer 1991; Ulloa et al. 1994). However, their actual contributions under different conditions in various aquatic environments are certainly variable and remain difficult to ascertain (Stramski et al. 2004*a*; Stramski and Woźniak 2005).

In agreement with previous studies of viral lysis of heterotrophic bacteria (Shibata et al. 1997; Balch et al. 2002), we observed a rapid collapse of the host bacterial population associated with an increase in the abundance of viruses, the formation of submicron material as hosts were disrupted and cell debris released, and clearing of the infected culture (as quantified by a drastic decrease in the particulate scattering coefficient). The potential optical implications of this observation for aquatic environments involve an increase in the clarity of water and changes in light fields within and leaving the waterbody. In particular, the light would propagate deeper through the water column, which naturally has significance for marine photochemistry and ecology. It is reasonable to expect that such effects might be detectable optically under conditions of massive viral infection and lysis of host cells (Balch et al. 2002; Simis et al. 2005).

By using a combination of several techniques for particle sizing, we made determinations of the PSD over four orders of magnitude in particle size during the course of the experiment. Acquiring such comprehensive PSD data is essential for an understanding of particle dynamics and the consequent changes in the optical properties, yet to our knowledge such acquisition has not been achieved in the past. A major finding from our study is that the viral infection causes remarkable changes in the PSD not only in the submicron size range but over the entire measured range (extending to 200 μm) and that these large changes occur over short timescales ranging from hours to a few days. Whereas at the beginning of the experiment the culture was dominated by bacteria, the particulate assemblage became more and more complex and diverse over time. In addition to the direct effects of viral infection leading to the breakdown of host population and formation of submicron particles, we observed a considerable increase in the concentration of large particles with sizes greater than ≈ 4 μm, which was especially well pronounced during the second and third days of the experiment. This is evidence for aggregation of smaller sized particles, including the colloidal fraction. Thus, our results show that the lytic viral infection of bacteria can potentially contribute to the transformation of the PSD beyond the small size range of viruses, hosts, and immediate lysis products. Because of the inherent limitations of laboratory experimental conditions we cannot make definite conclusions about the roles of such aggregation processes in natural aquatic environments. Nevertheless, our results indicate a need for future studies on the potential of viral lysis products as seeds for particle aggregation in the ocean. This question would be of particular interest considering the significant role of particle aggregates in the export of particulate matter into the deep ocean and as hotspots for microbial growth and carbon remineralization (McCave 1984; Alldredge et al. 1986; Azam and Long 2001).

The development of understanding of optical contributions by different particle size classes within polydisperse assemblages has typically involved the use of idealized shapes of PSD or incomplete particle size data (e.g., Stramski and Kiefer 1991; Simis et al. 2007). Such approaches are naturally subject to uncertainties that limit this understanding. Our experiment provides evidence that dynamic biological interactions can produce large changes in PSD, the shape of which is not adequately described by some simple approximations over the extended size range, such as a power function with a single slope. By using the measured PSDs covering four orders of magnitude in particle size as input to the Mie scattering model, we estimated the relative contributions of different size classes to scattering properties during the course of our experiment. These results support the notion that within dynamically interacting populations of biological particles

the optical roles of specific particle types can vary on short timescales from negligible or small to dominant, depending on their relative abundances. For example, whereas the estimated contribution of large particles (> 4 μm in size) to the particulate scattering coefficient of infected culture was very small at the beginning of the experiment, these particles dominated scattering 72 h after infection.

Acknowledgments

This study was supported by the Division of Ocean Sciences, National Science Foundation (grant OCE04-28900, awarded to D.S. and F.A.), the U.S. Office of Naval Research Environmental Optics Program (grant N00014-05-1-0246, awarded to D.S.), and the Gordon and Betty Moore Foundation Marine Microbiology Initiative (grant awarded to F.A.). We thank two anonymous reviewers for comments on the manuscript.

References

Agrawal, Y. C., and H. C. Pottsmith. 2000. Instruments for particle size and settling velocity observations in sediment transport. Mar. Geol. **168:** 89–114, doi:10.1016/S0025-3227(00)00044-X

Alldredge, A. L., J. J. Cole, and D. A. Caron. 1986. Production of heterotrophic bacteria inhabiting macroscopic organic aggregates (marine snow) from surface waters. Limnol. Oceanogr. **31:** 68–78, doi:10.4319/lo.1986.31.1.0068

Azam, F., and R. A. Long. 2001. Oceanography—sea snow microcosms. Nature **414:** 495–498, doi:10.1038/35107174

———, and F. Malfatti. 2007. Microbial structuring of marine ecosystems. Nat. Rev. Microbiol. **5:** 782–791, doi:10.1038/nrmicro1747

Babin, M., and D. Stramski. 2002. Light absorption by aquatic particles in the near-infrared spectral region. Limnol. Oceanogr. **47:** 911–915, doi:10.4319/lo.2002.47.3.0911

———, and ———. 2004. Variations in the mass-specific absorption coefficient of mineral particles suspended in water. Limnol. Oceanogr. **49:** 756–767, doi:10.4319/lo.2004.49.3.0756

Balch, W. M., J. M. Vaughn, J. I. Goes, J. F. Novotny, D. T. Drapeau, E. Booth, and C. L. Vining. 2007. Bio-optical consequences of viral infection of phytoplankton: I. Experiments with the cyanobacterium, *Synechococcus* sp. Limnol. Oceanogr. **52:** 727–738, doi:10.4319/lo.2007.52.2.0727

———, ———, J. F. Novotny, D. T. Drapeau, R. D. Vaillancourt, J. M. Lapierre, and A. Ashe. 2000. Light scattering by viral suspensions. Limnol. Oceanogr. **45:** 492–498, doi:10.4319/lo.2000.45.2.0492

———, and others. 2002. Fundamental changes in light scattering associated with infection of marine bacteria by bacteriophage. Limnol. Oceanogr. **47:** 1554–1561, doi:10.4319/lo.2002.47.5.1554

Bettarel, Y., and others. 2008. Virioplankton distribution and activity in a tropical eutrophicated bay. Estuar. Coast. Shelf Sci. **80:** 425–429, doi:10.1016/j.ecss.2008.08.018

Bohren, C. F., and D. R. Huffman. 1983. Absorption and scattering of light by small particles. Wiley.

Boss, E., M. S. Twardowski, and S. Herring. 2001. Shape of the particulate beam attenuation spectrum and its inversion to obtain the shape of the particulate size distribution. Appl. Opt. **40:** 4885–4893, doi:10.1364/AO.40.004885

Bricaud, A., A. L. Bédhomme, and A. Morel. 1988. Optical properties of diverse phytoplanktonic species: Experimental results and theoretical interpretation. J. Plankton Res. **10:** 851–873, doi:10.1093/plankt/10.5.851

Chin, W. C., M. V. Orellana, and P. Verdugo. 1998. Spontaneous assembly of marine dissolved organic matter into polymer gels. Nature **391:** 568–572, doi:10.1038/35345

Cho, B. C., and F. Azam. 1990. Biogeochemical significance of bacterial biomass in the ocean's euphotic zone. Mar. Ecol. Prog. Ser. **63:** 253–259, doi:10.3354/meps063253

Clavano, W. R., E. Boss, and L. Karp-Boss. 2007. Inherent optical properties of non-spherical marine-like particles—from theory to observation, p. 1–38. *In* R. N. Gibson, R. J. A. Atkinson and J. D. M. Gordon [eds.], Oceanography and marine biology. V. 45. CRC Press.

Floge, S. A., and M. L. Wells. 2007. Variation in colloidal chromophoric dissolved organic matter in the Damariscotta Estuary, Maine. Limnol. Oceanogr. **52:** 32–45, doi:10.4319/lo.2007.52.1.0032

Giddings, J. C. 1993*a*. Field-flow fractionation: Analysis of macromolecular, colloidal, and particulate materials. Science **260:** 1456–1465, doi:10.1126/science.8502990

———. 1993*b*. Retention (steric) inversion in field-flow fractionation: Practical implications in particle-size, density and shape-analysis. Analyst **118:** 1487–1494, doi:10.1039/an9931801487

Haardt, H., and H. Maske. 1987. Specific in vivo absorption-coefficient of chlorophyll *a* at 675 nm. Limnol. Oceanogr. **32:** 608–619, doi:10.4319/lo.1987.32.3.0608

Johnsen, G., O. Samset, L. Granskog, and E. Sakshaug. 1994. In vivo absorption characteristics in 10 classes of bloom-forming phytoplankton: Taxonomic characteristics and responses to photoadaptation by means of discriminant and HPLC analysis. Mar. Ecol. Prog. Ser. **105:** 149–157, doi:10.3354/meps105149

Jonasz, M. 1987. Nonsphericity of suspended marine particles and its influence on light-scattering. Limnol. Oceanogr. **32:** 1059–1065, doi:10.4319/lo.1987.32.5.1059

———, and G. R. Fournier. 2007. Light scattering by particles in water, theoretical and experimental foundations. Elsevier.

Li, W. K. W. 1998. Annual average abundance of heterotrophic bacteria and *Synechococcus* in surface ocean waters, Limnol. Oceanogr. **43:** 1746–1753.

Long, R. A., and F. Azam. 2001. Antagonistic interactions among marine pelagic bacteria. Appl. Environ. Microbiol. **67:** 4975–4983, doi:10.1128/AEM.67.11.4975-4983.2001

Lyven, B., M. Hassellov, C. Haraldsson, and D. R. Turner. 1997. Optimisation of on-channel preconcentration in flow field-flow fractionation for the determination of size distributions of low molecular weight colloidal material in natural waters. Anal. Chim. Acta **357:** 187–196, doi:10.1016/S0003-2670(97)00565-5

Malfatti, F., T. J. Samo, and F. Azam. 2010. High-resolution imaging of pelagic bacteria by atomic force microscopy and implications for carbon cycling. ISME J. **4:** 427–439, doi:10.1038/ismej.2009.116

McCave, I. N. 1984. Size spectra and aggregation of suspended particles in the deep ocean. Deep-Sea Res. I **31:** 329–352, doi:10.1016/0198-0149(84)90088-8

Mishchenko, M. I., J. W. Hovenier, and L. D. Travis. 2000. Light scattering by nonspherical particles. Theory, measurements, and applications. Academic Press.

Morel, A., and Y. H. Ahn. 1991. Optics of heterotrophic nanoflagellates and ciliates: A tentative assessment of their scattering role in oceanic waters compared to those of bacterial and algal cells. J. Mar. Res. **49:** 177–202, doi:10.1357/002224091784968639

———, and A. Bricaud. 1986. Inherent optical properties of algal cells including picoplankton: Theoretical and experimental results. Can. Bull. Fish. Aquat. Sci. **214:** 521–560.

Noble, R. T., and J. A. Fuhrman. 1998. Use of SYBR Green I rapid epifluorescence counts of marine viruses and bacteria. Aquat. Microb. Ecol. **14:** 113–118, doi:10.3354/ame014113

Sathyendranath, S., L. Lazzara, and L. Prieur. 1987. Variations in the spectral values of specific absorption of phytoplankton. Limnol. Oceanogr. **32:** 403–415, doi:10.4319/lo.1987.32.2.0403

Shibata, A., K. Kogure, I. Koike, and K. Ohwada. 1997. Formation of submicron colloidal particles from marine bacteria by viral infection. Mar. Ecol. Prog. Ser. **155:** 303–307, doi:10.3354/meps155303

Simis, S. G. H., M. Tijdens, H. L. Hoogveld, and H. J. Gons. 2005. Optical changes associated with cyanobacterial bloom termination by viral lysis. J. Plankton Res. **27:** 937–949, doi:10.1093/plankt/fbi068

———, ———, ———, and ———. 2007. Optical signatures of the filamentous cyanobacterium *Leptolyngbya boryana* during mass viral lysis. Limnol. Oceanogr. **52:** 184–197, doi:10.4319/lo.2007.52.1.0184

Stramski, D., E. Boss, D. Bogucki, and K. J. Voss. 2004*a*. The role of seawater constituents in light backscattering in the ocean. Prog. Oceanogr. **61:** 27–56, doi:10.1016/j.pocean.2004.07.001

———, A. Bricaud, and A. Morel. 2001. Modeling the inherent optical properties of the ocean based on the detailed composition of the planktonic community. Appl. Opt. **40:** 2929–2945, doi:10.1364/AO.40.002929

———, and D. A. Kiefer. 1991. Light scattering by microorganisms in the open ocean. Prog. Oceanogr. **28:** 343–383, doi:10.1016/0079-6611(91)90032-H

———, and J. Piskozub. 2003. Estimation of scattering error in spectrophotometric measurements of light absorption by aquatic particles from three-dimensional radiative transfer simulations. Appl. Opt. **42:** 3634–3646, doi:10.1364/AO.42.003634

———, F. Rassoulzadegan, and D. A. Kiefer. 1992. Changes in the optical properties of a particle suspension caused by protist grazing. J. Plankton Res. **14:** 961–977, doi:10.1093/plankt/14.7.961

———, and S. B. Woźniak. 2005. On the role of colloidal particles in light scattering in the ocean. Limnol. Oceanogr. **50:** 1581–1591, doi:10.4319/lo.2005.50.5.1581

———, ———, and P. J. Flatau. 2004*b*. Optical properties of Asian mineral dust suspended in seawater. Limnol. Oceanogr. **49:** 749–755, doi:10.4319/lo.2004.49.3.0749

Suttle, C. A. 2005. Viruses in the sea. Nature **437:** 356–361, doi:10.1038/nature04160

Twardowski, M. S., E. Boss, J. B. MacDonald, W. S. Pegau, A. H. Barnard, and J. R. V. Zaneveld. 2001. A model for estimating bulk refractive index from the optical backscattering ratio and the implications for understanding particle composition in case I and case II waters. J. Geophys. Res. **106:** 14129–14142, doi:10.1029/2000JC000404

Ulloa, O., S. Sathyendranath, and T. Platt. 1994. Effect of the particle-size distribution on the backscattering ratio in seawater. Appl. Opt. **33:** 7070–7077, doi:10.1364/AO.33.007070

Vaillancourt, R. D., and W. M. Balch. 2000. Size distribution of marine submicron particles determined by flow field–flow fractionation. Limnol. Oceanogr. **45:** 485–492, doi:10.4319/lo.2000.45.2.0485

———, C. W. Brown, L. R. R. Guillard, and W. M. Balch. 2004. Light backscattering properties of marine phytoplankton: Relationships to cell size, chemical composition and taxonomy. J. Plankton Res. **26:** 191–212, doi:10.1093/plankt/fbh012

Verdugo, P., A. L. Alldredge, F. Azam, D. L. Kirchman, U. Passow, and P. H. Santschi. 2004. The oceanic gel phase: A bridge in the DOM-POM continuum. Mar. Chem. **92:** 67–85, doi:10.1016/j.marchem.2004.06.017

Volten, H., and others. 1998. Laboratory measurements of angular distributions of light scattered by phytoplankton and silt. Limnol. Oceanogr. **43:** 1180–1197, doi:10.4319/lo.1998.43.6.1180

von der Kammer, F., M. Baborowski, and K. Friese. 2005. Field-flow fractionation coupled to multi-angle laser light scattering detectors: Applicability and analytical benefits for the analysis of environmental colloids. Anal. Chim. Acta **552:** 166–174, doi:10.1016/j.aca.2005.07.049

Wells, M. L. 2004. The colloidal size spectrum of CDOM in the coastal region of the Mississippi plume using flow field–flow fractionation. Mar. Chem. **89:** 89–102, doi:10.1016/j.marchem.2004.02.009

Wyatt, P. J. 1998. Submicrometer particle sizing by multiangle light scattering following fractionation. J. Coll. Interface Sci. **197:** 9–20, doi:10.1006/jcis.1997.5215

Zanardi-Lamardo, E., C. A. Moore, and R. G. Zika. 2004. Seasonal variation in molecular mass and optical properties of chromophoric dissolved organic material in coastal waters of southwest Florida. Mar. Chem. **89:** 37–54, doi:10.1016/j.marchem.2004.02.018

Zaneveld, J. R. V., and J. C. Kitchen. 1995. The variation in the inherent optical properties of phytoplankton near an absorption peak as determined by various models of cell structure. J. Geophys. Res. **100:** 13309–13320, doi:10.1029/95JC00451

Associate editor: Heidi M. Sosik

Received: 22 December 2009
Accepted: 15 June 2010
Amended: 20 July 2010